Batteries & Supercaps

Articles
doi.org/10.1002/batt.202100132

Chemistry
Europe
European Chemical
Societies Publishing

"Less is More": Ultra Low LiPF$_6$ Concentrated Electrolyte for Efficient Li-Ion Batteries

Georgios Nikiforidis[a, b, c] and Mérièm Anouti*[a, b]

In the pursuit of lowering the cost of lithium-ion (LIB) and lithium-metal batteries (LMB), we reduced the lithium salt concentration of the electrolyte (i.e., lithium hexafluorophosphate LiPF$_6$) to a record low 0.1 mol L^{-1} LiPF$_6$. Herein we present the performance of lithium nickel manganese cobalt oxide (NMC), lithium manganese oxide (LMO), lithium iron phosphate (LFP) cathodes together with graphite and lithium metal anodes in a ternary solvent mixture of ethylene carbonate (EC), ethyl methyl carbonate (EMC), and 1,1,2,2-tetrafluoroethyl 2,2,2-trifluoroethyl ether (TFE) (3EC/7EMC/20TFE, by weight) containing 0.1 mol L^{-1} LiPF$_6$. By virtue of the favored ionic associations between Li$^+$ and PF$_6^-$ in the presence of the TFE together with EC and EMC, the half and full coin cells revealed a robust performance at room temperature with high specific capacities

and coulombic efficiencies ($>$98.5%) over a wide current range (C/2→2C), high capacity retention, modest energy density (180 to 207 Wh kg^{-1} depending on the system), extended calendar life (600 h for the Li symmetric cells), and superior operation to cells using commercial carbonate electrolytes (i.e., 1 mol L^{-1} LiPF$_6$ in EC/EMC, 3/7, v/v). The morphological characterization of the electrodes revealed mild structural degradation, homogenous distribution of the electrode and electrolyte-based elements, as well as the formation of decomposition products, especially for the graphite anode. Overall, this study attests to the compatibility of low-concentrated Li salt electrolytes with promising cathode and anode materials for efficient and cost-effective battery systems.

1. Introduction

As the immediacy of the climate crisis becomes ever more apparent, batteries are instrumental for the transition towards a carbon-neutral economy, facilitating the decarbonization of the transportation sector (e.g., hybrid electric vehicles, HEVs, plug-in hybrid electric vehicles, PHEVs, and all-electric vehicles EVs),[1] balancing power grids and saving surplus energy from intermittent solar and wind power generation,[2] and being integrated into utility companies' systems, such as hospitals and natural gas plants. Over the last decade, the most prolific battery technology: lithium-ion, has incurred an 85% decline in price[3] as production has reached economy of scale, making electric vehicles and stationary energy storage commercially viable for the first time in history.[4] Total battery capacity in stationary applications is expected to increase from a current estimate of 11 GWh to between 100 and 167 GWh in 2030.[5] LIB current price lies at $137/kWh[3] and is projected to reach below $100/kWh in the next years, achieving price parity with internal combustion engines.[6] Strategies associated with the increase of electrode thickness to boost the current power level

(4 mAh cm^{-2}), the reduction of the solid electrolyte interface (SEI) layer formation time, the improvement of the anode electrolyte wetting, and the mitigation of the use of N-methyl pyrrolidone dispersion for cathode production, aspire to condense the battery cost production further.[7]

The main components of a battery include the anode, cathode, separator, and electrolyte. State-of-the-art LIBs comprise lithium-rich transition-metal oxide cathodes, of which an array of materials have been reported[8] aiming to enhance their limited specific capacity. The charge storage capacity of the oxide host is restricted to the reversible solid-solution range of Li$^+$ intercalation in the cathode host structure on the redox energy of a single metal transition cation.[9] The anode electrodes in LIBs comprise graphite, lithium titanate oxide (LTO), and other alloys such as Si and SiO$_2$.[8] Here, a Li$^+$-permeable passivating layer forms during the first charge (i.e., solid electrolyte interphase, SEI), leading to irreversible loss of Li from the cathode.[10] Nonetheless, the broad applicability of LIBs is advocated on account of their moderate energy density (200 Wh kg^{-1}), high energy efficiency ($>$97%), and long calendar life (i.e., 3000 cycles at 80% DOD).[11] Metallic current collectors deliver electronic current from the redox centers of the electrodes to terminals connected to the external circuit and vice versa. Fabricated in the discharged state, the cell is activated by the charging process, during which the cathode is oxidized to produce Li$^+$ and electrons (e$^-$). The Li$^+$ travels through the electrolyte towards the anode, where it gets reduced with the e$^-$ arriving through the external circuit. The opposite process takes place during discharge.

LIB's volumetric and gravimetric energy densities stem from the high cell voltage (between 3 and 5 V), instantly rendering safety the most critical operating parameter. Commercial LIBs

[a] Dr. G. Nikiforidis, Prof. M. Anouti
Laboratoire PCM2E, Université de Tours
Parc de Grandmont, 37200, Tours, France
E-mail: meriem.anouti@univ-tours.fr
[b] Dr. G. Nikiforidis, Prof. M. Anouti
LE STUDIUM Institute for Advanced Studies
45000, Orléans, France
[c] Dr. G. Nikiforidis
Department of Biomedical Engineering, Northwestern University
Evanston, IL, 60208, USA

have adopted organic liquids such as aliphatic ethers and carbonates as electrolyte solvents; such organic electrolytes have a wide electrochemical window and, under ideal operating conditions, are nonflammable, safe, and functional. Currently, LIBs employ dimethyl carbonate (DMC), diethyl carbonate (DEC), propylene carbonate (PC), ethylene carbonate (EC), and ethyl methyl carbonate (EMC)[12] as electrolyte solvents. When EC and DMC, or other aliphatic linear carbonates, are mixed, a synergistic effect is realized as each solvent imparts its merits to the resulting mixture. More specifically, the high anodic stability of EC on cathode surfaces and its high solubility towards Li salts, and the low viscosity of linear carbonates that promote ionic conductivity.[13] To effectuate a functional electrolyte, a conducting salt, most commonly lithium hexafluorophosphate ($LiPF_6$), lithium tetrafluoroborate ($LiBF_4$), and lithium perchlorate ($LiClO_4$), is dissolved in the solvent mixture, usually in concentrations of $1 \, mol \, L^{-1}$.[14] This concentration is generally selected because it yields the highest conductivity and provides a sufficient amount of Li ions to buffer their potential loss during the battery cycling. When the cells are exposed to mechanical, thermal, or electrical abuse conditions, their safety is compromised; the cell temperature can rise high enough to cause the electrolyte solvent to evaporate, increasing the pressure in the cell and propagating In order to comply with the high energy and safety requirements, LIB electrolytes should fulfill the following criteria:[13,15] i) low viscosity, high ionic conductivity, and high dielectric constant, ii) stability over a wide electrochemical window and operating temperature range, iii) chemical and electrochemical inertness towards battery components (i.e., separator, current collectors, packaging materials), iv) formation of effective SEI and CEI (cathode electrolyte interface) layers after initial cycling, which will mitigate electrolyte decomposition and prolong cycle life and v) wide liquidus range.

In the interest of the mitigation of electrolyte flammability, the reduction of gas generation during SEI formation, and the increase of thermal stability, a myriad of electrolyte additives in quantities within 5 wt.% or v/v% have been reported as performance boosters for the LIB.[16] Following a somewhat different strategy, we focused on a cost-friendly alternative to achieve such improvements by adding TFE (1,1,2,2-tetrafluoroethyl 2,2,2-trifluoroethyl ether) as a co-solvent in an EC/EMC electrolyte solvent mixture. The novel ternary solvent mixture comprising EC/EMC and TFE (1,1,2,2-tetrafluoroethyl 2,2,2-trifluoroethyl ether) with a weight ratio of 3/7/20 under a salt concentration of $0.1 \, mol \, L^{-1}$ $LiPF_6$ has recently demonstrated its feasibility of LIB applications.[17] We tested the performance of this nonflammable quaternary fluorinated electrolyte on nickel manganese cobalt NMC (111)-graphite pouch cells where their performance was superior to identical cells containing commercial electrolyte, exhibiting a specific capacity of $165 \, mAh \, g^{-1}$, capacity retention over 90%, and a coulombic efficiency of 99.2% over 700 deep cycles. The use of fluorinated electrolytes has been previously reported in LIBs (e.g., $1.0 \, mol \, L^{-1}$ $LiPF_6$ in fluoroethylene carbonate, 3,3,3-fluoroethylmethyl carbonate, and 1,1,2,2-tetrafluoroethyl-2′,2′,2′-trifluoroethyl ether, 2:6:2 by weight)[18] where the formation of a fluorinated nanolayer interphase acted beneficially for the performance of the battery. Yet, never in such low salt concentrations.

While NMC is one of the most successful layered cathode materials owing to their high specific energy, low weight, and safety, for robust and reliable LIBs,[19] other cathodes are equally promising in terms of cost, calendar life, and safety, such as lithium manganese oxide (LMO, $LiMn_2O_4$) and lithium iron phosphate (LFP, $LiFePO_4$). LMO has a spinel crystal structure with a 3D network of interconnected interstitial sites for efficient and rapid Li^+ transport,[20] with a lithium extraction ratio as high as 0.6 ($Li_{1-x}Mn_2O_4$ for $0 < x < 0.6$). It bears a high specific power, long calendar life (1500 cycles), moderate energy density ($130 \, Wh \, kg^{-1}$), low cost (Co-free), and is safe (thermal runaway occurs at 250 °C).[21] LFP is also inherently safe, durable (2000 cycles), cheap, allows for deep charge-discharge cycling (15%–100% SOC), and carries a specific energy of ca. $110 \, Wh \, kg^{-1}$.[21] Here, the use of phosphates avoids concerns of environmental contamination of cobalt. LFP has a similar lithium extraction ratio to LMO (0.6) at a closed-circuit voltage of 3.5 V vs. Li/Li^+, holds an extended voltage platform, and bears no structural changes upon the intercalation/deintercalation process (i.e., ordered olivine structure) due to its strong P–O bond in the space lattice.[22] Regarding the anode, aside from the ubiquitous graphite electrode ($372 \, mAh \, g^{-1}$, $900 per ton),[23] the implementation of Li metal is much sought-after due to its high capacity ($3860 \, mAh \, g^{-1}$) and low standard negative electrochemical potentials (−3.040 V).[24] The scarcity, and hence cost, of the highly reactive Li[25] together with its proneness to dendritic growth, hinder the further deployment of lithium metal batteries (LMBs). Nonetheless, several studies and seminal reviews have manifested a recent revival of research and development for LMBs.[24,26]

In this paper, we studied the performance of the newly reported ternary solvent mixture (EC/EMC/TFE) on half and full-cell coin cells comprising NMC, LMO, LFP cathodes, and Li metal anodes (in the form of Li symmetric cells), thus assessing the feasibility of the use of our electrolyte for high-energy dense and safe batteries. We initially characterized the ternary fluorinated electrolyte properties (molar conductivity, ionic conductivity, and viscosity) to delineate the ion-pair dissociation coefficient. Then, we conducted a series of electrochemical tests (galvanostatic charge-discharge, potentioelectrochemical impedance spectroscopy, cyclic voltammetry) at room temperature and proceeded with surface analyses (scanning electron microscopy, SEM, energy dispersive X-ray spectroscopy, EDX, Fourier-transform infrared spectroscopy, FT-IR and X-ray diffraction, XRD) of the electrodes and separators before and after long term operation on both ternary-low salt and standard electrolytes. The results stemmed from this study corroborate the use of low Li salt concentrated ternary and nonflammable electrolytes for robust and cost-effective LIBs and LMBs.

2. Results and Discussion

2.1. Quaternary Fluorinated Electrolyte Properties

The ionic conductivity σ, as a function of Li salt concentration (C) and temperature, is portrayed in Figure 1(a). The evolution of the ionic conductivity with $LiPF_6$ reaches a maximum (σ_{max}) close to 0.8 mol L^{-1}. C_{max} largely depends on the nature of the salt and, to a lesser extent to the solvent's nature. For instance, C_{max} is equal to 1.00 mol L^{-1} $LiPF_6$ in a EC/DMC solution,[27] 1.16 mol L^{-1} LiTFSI in EC/DMC, 0.70 mol L^{-1} for LiTDI[27] and 1.28 mol L^{-1} for KPF_6,[28] in the same binary carbonate solvent. Figure 1(b) shows the conductivity of the quaternary fluorinated mixture as a function of $LiPF_6$ concentration of (0.1 to 1.0 mol L^{-1}) and compares it to the standard 1 mol L^{-1} $LiPF_6$ solution in EC/EMC (3/7, v/v). The solution with the minimum salt concentration (0.1 mol L^{-1}) retains a conductivity value of 0.6 mS cm^{-1}. This value increases with salt concentration and reaches 1.5 mS cm^{-1} at 25 °C, about 8 times lower than the conductivity of the standard electrolyte.

The ion-pair dissociation coefficients of $LiPF_6$ (α_D) were estimated using experimental data together with the empirical relationship[29] $\alpha_D = (\Lambda\eta)/(\Lambda_0\eta_0)$, where Λ and η describe the measured molar conductivity and viscosity at a set temperature, and Λ_0 and η_0 represent the limiting molar conductivity at high dilution and the solvent viscosity, respectively. The Λ_0 values were extrapolated in highly diluted conditions (i.e., C approaching 0 mol L^{-1}) where the variations of Λ against $C^{1/2}$ obey the Debye-Hückel-Onsager relationship,[30] viz. $\Lambda = \Lambda_0 - b \times C^{1/2}$, (Figure 1c). The dissociation coefficients (Table 1) are similar to those of standard carbonate electrolytes, i.e., 1 mol L^{-1} $LiPF_6$ in EC/DMC.[27,28] What's more, the unexpected drop of α_D with decreased C values indicates that the Li^+-PF_6^- dissociation at these concentrations is not the predominant factor in the transport of the Li^+ cation unlike other alkylcarbonates.[27] Thus, we postulate that there is good coordination of the Li cations with TFE, which opposes the complete dissociation of $LiPF_6$ and solvation of the Li ions by the EC molecule in solution, especially at lower salt concentrations. Indeed, the computational calculation energy by molecular orbital optimization of the EC-Li and TFE-Li dual
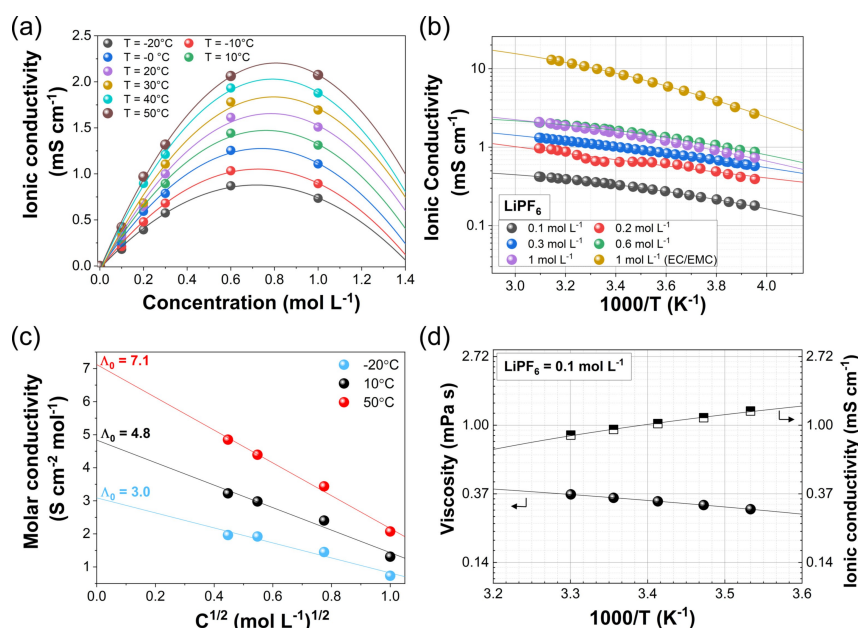

Figure 1. Physiochemical properties of the quaternary fluorinated electrolyte. (a) Ionic conductivity at various temperatures as a function of salt concentration. (b) Arrhenius plot of ionic conductivity and compared against a standard electrolyte (1 mol L^{-1} $LiPF_6$ in EC/EMC, 3/7, v/v). (c) Molar conductivity at different temperatures vs. square root of salt concentration (C). (d) Logarithmic plot of the conductivity and viscosity as a function of 1000/T for $C = 0.1$ mol L^{-1} $LiPF_6$ in EC/EMC/TFE (3/7/20, wt).

Table 1. Molar conductivity Λ, limiting molar conductivity, Λ_0, viscosity, η and ion-pair dissociation coefficient as a function of temperature, T, for 0.1 and 0.2 mol L^{-1} $LiPF_6$ in EC/EMC/TFE.

T [°C]	Concentration [mol L^{-1}]	Λ [S cm^2 mol^{-1}]	Λ_0 [S cm^2 mol^{-1}]	η [mPa s]	α_D
10	0.1	2.95	4.8	1.23	0.64
	0.2	3.59		1.28	0.81
20	0.1	3.30	5.0	1.02	0.69
	0.2	3.98		1.06	0.86
30	0.1	3.65	5.5	0.86	0.70
	0.2	4.42		0.89	0.88

complexes (Supporting Information, Table S1) uncovered dynamic interactions between TFE and Li cations within the electrostatic potential of the TFE molecule, which is not the case for the EC-Li complex. Thus, the Li cations are more accessible to intercalate/de-intercalate from TFE-Li dual complexes than EC-Li ones.

As a final point, the changes in η and σ for the electrolyte containing 0.1 mol L^{-1} LiPF$_6$ (Figure 1d) pinpoint an Arrhenius behavior. It has been previously reported[17] that the energy barrier of ion mobility in the presence of TFE is independent of concentration. It remains close to 8 kJ mol^{-1}, not far off the energy barrier of infinitely diluted standard electrolytes. We, therefore, propose a salt dissociation scheme that is partly solvated by alkylcarbonates and, at the same time, complexed by TFE (Table S1).

2.2. Half-Cells

2.2.1. Graphite-Li Half-Cell

For the graphite-Li metal half-cell, the cut-off voltage was set to 7.5 mV for discharge (i.e., lithiation) and 2.5 V for charge (i.e., delithiation). A 1C rate corresponds to 372 mA g^{-1} on the weight basis of graphite. Figure S1(a) confirms the reversible Li$^+$ intercalation at a C/20 rate. The graphite electrode demonstrated a capacity of 325 mAh g^{-1} at a C/10 rate (Figure 2a and Figure S1b), close to the theoretical capacity based on fully lithiated LiC$_6$. The typical low potential plateaus represent the sequential formation of several stage structures of the Li-graphite intercalation compounds.[31] At a higher rate (2C), the capacity was equal to 225 mAh g^{-1}. The rate capability of the graphite-Li half-cell is presented in Figure S1(c) at four different rates where the cell discharge specific capacity recovers to 278 mAh g^{-1} at a C/5 rate, 91% of its initial capacity. Upon repetitive cycling at a C/5 rate (Figure S1d), we encounter average coulombic efficiencies of 99.3% and capacity retention

of ca. 86%. The half-cell impedance increased noticeably, manifested by the broader semicircle of the Nyquist plot at 100 cycles (cycle 100, Figure S1e) against the plot at the first cycle. The semicircle takes into account the SEI film resistance (R_{SEI}) and the charge transfer resistance at the medium frequencies (R_{ct}, 18 Hz). After 100 cycles, R_{total} (ca. $R_1 + R_2$, where $R_2 = R_{SEI} + R_{ct}$) reaches 181 ohms compared to 142 ohms at cycle 1.

The XRD patterns of Figure S2(a, b) revealed sharp (002) diffraction peaks, characteristic of small d-spacing (i.e., orderly stacked layers).[32] The larger full width at half maximum (FWHM) of the pristine sample (0.184°) against the cycled one (0.111°) advocates for larger graphite crystallite sizes on the latter due to consecutive cycling. The SEM micrographs of the fresh and cycled anodes cycled with the quaternary fluorinated electrolyte at 25 °C are given in Figure S2(c–f). The pristine graphite surface comprises particles of different sizes (between 40 and 10 μm, Figure S2c). These irregular polyhedral particles are tightly in contact with each other and randomly arranged. After cycling, the surface showed moderate structural disintegration, and no drastic changes in its morphology are evident. Graphite particles are observed in the cycled anode (Figure S2d), covered by electrolyte decomposition products (the bright clusters we presume are Li metal, Figure S2e,f). As expected, to effectively passivate the graphite, electrolyte decomposition occurs as more reversible Li is consumed.[33] In brief, the formation of decomposition products is not absent in the low LiPF$_6$-concentrated electrolyte, nonetheless, the half-cell showed high coulombic efficiencies and resilient capacity retention for 100 cycles, in line with other graphite-Li metal half-cells.[34]

2.2.2. NMC-Li Half-Cell

The voltage profiles of the NMC-Li half-cell are shown in Figure 2(b). The cut-off voltage was set 2.9 V for discharge and 4.3 V for charge. The introduction of higher C rates (viz., 2C) delivers a specific capacity of 104 mAh g^{-1} (the theoretical capacity of NMC is ca. 274 mAh g^{-1} for 1C). The NMC-Li half-cell rate performance is illustrated in Figure S3(a), where the cell discharge specific capacity recovers to 145 mAh g^{-1}, 82% of its initial capacity at a C/5 rate. The cyclability of the cell is displayed in Figure S3(b) with average coulombic efficiencies of 98.75% throughout the 110 cycles, consistent with other reports.[35–38] The potentioelectrochemical impedance spectroscopy (PEIS) before and after cycling highlights the effect of long-term cycling. The electrical equivalent (EES) circuit describing the Nyquist plots is given in Figure S3(c), where R_1 corresponds to the distance between the left-side semicircle edge and the imaginary part axis, attributed to the electrolyte solution resistance within the cell, the contact resistance, and the resistance within the active materials.[39] Besides, a resistance and constant phase element (Q_2) related to the Li$^+$ migration through the surface film (R_2) is visualized as a small semicircle in the high to medium frequencies (0.5→0.05 MHz). A charge transfer resistance (R_3) and constant phase element (Q_3) are portrayed as a broad semicircle in the medium low-
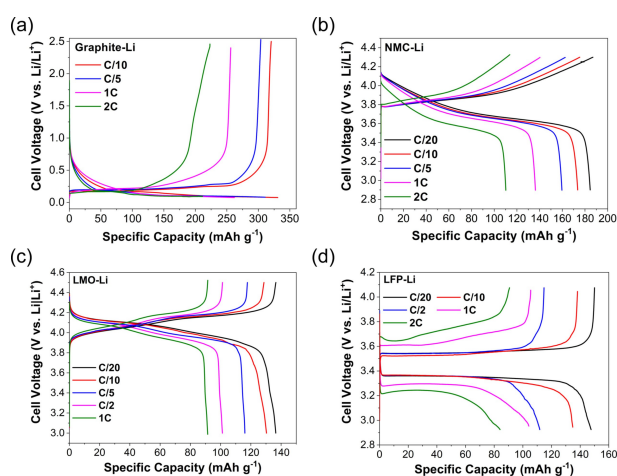

Figure 2. Voltage profiles at different rates for (a) the graphite-Li, (b) NMC-Li, (c) LMO-Li, and (d) LFP-Li half-cells in a solution containing 0.1 mol L^{-1} LiPF$_6$ in EC/EMC/TFE (3/7/20, wt). Cell operating temperature is 25 °C.

frequency region (3.5 kHz–0.07 Hz). With consecutive cycling, the film resistance (R_2) increased from 62.88 to 107.07 ohm (Table S2), suggesting sluggish Li^+ migration due to Li surface changes (e.g., formation of dead lithium, dendrites).[40] The change on the surface of the Li metal, in turn, hinders charge transfer, which increases with cycling (317.7→394.4 ohm, Table S2), a behavior evident in other reported NMC-Li half-cell studies.[41]

The pristine NMC surface exposed an irregular secondary particle morphology (Figure S4a,b) comprising microparticles with a complex size distribution. After cycling, the morphology is similar to that of the pristine sample, as seen by the localized SEM pictures of Figure S4(c,d). The XRD patterns of the NMC electrode before and after cycling are given in Figure S4(e) and correspond to the hexagonal R3 m space group of the NMC lattice.[42] There is an apparent splitting of the (006)/(012) pair of reflections in the pristine sample (i.e., good hexagonal ordering) as opposed to the cycled one. Still, the I(003)/I(104) peak intensity ratio for the pristine NMC was 1.43 compared to 1.54 for the cycled NMC, signifying that the bulk structure of the material is well maintained.[17] In short, the NMC cathode shows good performance and stability towards the proposed electrolyte in line with previous results.[17]

2.2.3. LMO-Li Half-Cell

Figure 2(c) presents the specific capacity of the LMO-Li half-cell at different C-rates. This cathode offers stable performance when operated between 3 and 4.3 V, with ~80% of the Li ions being utilized.[43] Here, the upper cut-off voltage was set to 4.5 V to use more Li ions and boost the cell capacity. In that sense, at C/20, the specific capacity reaches almost the theoretical capacity of the LMO, ca. 148 mAh g^{-1}, while upon the introduction of higher C-rates, it drops (e.g., 1C→ 90 mAh g^{-1}). The rate capability of the LMO-Li cell with the quaternary fluorinated electrolyte at five different rates ranging from C/10 to 1C is shown in Figure S5(a). The cell discharge capacity was ca. 123 mAh g^{-1} (87% capacity retention) when the current rate reverted to C/10. The quaternary fluorinated electrolyte shows better performance than the standard commercial electrolyte (i.e., control, 1 mol L^{-1} LiPF$_6$ in EC/EMC, 3/7, v/v) at a C/10 rate for 35 cycles (Figure 5b). The coulombic efficiency lingers at ~99%, and the capacity retention at this rate arrives at 86%. The cyclability of the half-cell is further supported in Figure S6(a,b) for 100 cycles of electrochemical Li de-insertion/insertion where the specific capacities were ca. 120 mAh g^{-1} for C/5, on par with literature.[43–45] The capacity deteriorated with cycling due to electrolyte decomposition (viz. high oxidative potential) and structural changes of the LMO occurring during cycling.[43] The feeble cycling stability emerges from the dissolution of Mn via a disproportionation reaction and the structural transformation from a cubic to tetragonal phase induced by the Jahn-Teller distortion due to the high spin state of Mn^{3+} during Li intercalation and deintercalation in the solid matrix.[46]

After cycling, the SEM pictures of the LMO electrode (Figure S7a,b) revealed a non-uniform surface with layered materials and clusters of LMO particles and dispersed binder.[20] The active material phase is depicted as particles in medium grey and the binder and carbon black mixture as the crinkly, sponge-like structures in light grey. On top of the above, there are pores distributed between the particles and binder.[47] The electrode's adhesion was not strong; the inorganic surface was quite brittle. The LMO particles exposed loose contact and cracks, leading to elevated cell resistance, corroborated from PEIS (Figure S5c). The fitted electrical equivalent circuit (EEC) consists of a resistor R_1 in series with two parallel R/Q combinations ($R_2 + Q_2$, $R_3 + Q_3$, inset of Figure S5c). The EEC elements are described as follows:[48] R_1 is ascribed to the ion transport inside the separator and the electrolyte; the R_2 and Q_2 combination denotes lithium migration through the SEI layer, and the R_3 and Q_3 group reflects the charge-transfer at the electrode/electrolyte interface. The Nyquist plots of the aged cells depicted a broader semicircle in the medium to low frequencies (0.05 MHz–10 Hz, Table S3, R_2), characteristic of a sluggish Li ion migration through the film and a deteriorated electrode/electrolyte interface.

The XRD patterns (Figure S7) of the pristine and cycled LMO attest to spinel LMO in a pure cubic phase belonging to the Fd-3m space group.[49] The (111) plane of cubic spinel LMO gave the highest intensity (Figure S7a), pointing to a preferred growth direction along the (111) reflection plane. The (511), (531), (331), (222), and (440) planes of the cycled LMO are not as strong and sharp as the ones of the pristine LMO (Figure S7b). The absence of characteristic peaks of other phases (e.g., (220)) in the spectra asserts the absence of impurities in the pristine and cycled electrodes. The XRD patterns have a high intensity ratio of (111) and (311) reflection planes (viz., I(111)/I(311) ≈ 1.5). Besides, the full width at half maximum (FWHM) of the (400) peak (FWHM$_{pristine}$ = 0.210° vs. 0.271° and 0.245° of the LMO 50 and 30 cycles, respectively) connoted the crystallinity of the spinel structure with the Li ions occupying tetrahedral positions.[49,50] Overall, PEIS, SEM, and XRD results confirmed the inevitable aging of the half-cell under the quaternary fluorinated electrolyte; however, not in a worse state than other reported studies[43,44] and certainly superior to the standard electrolyte.

2.2.4. LFP-Li Half-cell

The specific capacity as a function of cell voltage of the LFP-Li half-cell between 2.9 and 4.2 V at different C-rates (C/20, C/10, C/2, 1C, and 2C) is given in Figure 2(d), in the presence of the quaternary fluorinated electrolyte. The LFP half-cell yielded a specific capacity of 151 mAh g^{-1} at a C/20 rate, close to the theoretical capacity of LFP (viz. 170 mAh g^{-1}).[51,52] At higher C-rates (2C), the capacity fell to 92 mAh g^{-1} (33% decline). The cycling performance is measured for 120 cycles at different C-rates. The specific capacity decreased from 138 at the initial cycle to 125 mAh g^{-1} at the 60th cycle, with a capacity loss of 9% at a C/10 rate (Figure S8a). A more noticeable capacity loss

(i.e., 19%) is evident for the successive 60 cycles where the current rate is set at C/5. Still, the performance is marginally better to the cells containing the standard commercial electrolyte.

PEIS performed at the beginning, middle, and end of cycling (Figure S8b) communicated a broad semicircle covering the high and middle frequency regions and a straight line in the low-frequency region (7 Hz). The wide semicircle describes the charge transfer resistance (R_{ct}) that increased from 169 to 223 and 281 ohm at the 60th and 120th cycles. In addition, the crystal structures of the LFP cathode before and after cycling were probed by X-ray diffraction. The presence of distinct diffraction peaks in the LFP patterns are allocated to the orthorhombic structure with a Pnma space group[53] and are assigned to pure LFP patterns[54] (Figure S8c). The profiles of the reflection peaks are narrow, signifying high crystallinity. The absence of typical carbon diffraction peaks indicates that the carbon coatings are amorphous. At the end of the cycling protocol, the LFP diffraction peaks exposed the formation of impurity phases, namely Li_3PO_4, Fe_2O_3, and FeP_2 (Figure S8c), stemming from the Fe deficiency in the $LiFePO_4$ crystal lattice,[55] which in turn, explains the capacity fading within high C-rates.

The surface morphology of pristine LFP comprised irregular ellipsoid particles with ~1–5 μm in diameter, bearing a nano-sized spindle-like morphology with an uneven particle distribution (Figure S9a, b). The LFP particles are dispersed among the smaller PVDF conducting agent. The morphology and microstructure of the amorphous LFP are similar to the pristine one after cycling (Figure S9c, d). Yet, the presence of bigger particles and agglomerates is evident on the surface of the electrode, potentially due to cycling. The elemental mapping analysis of the cycled electrode (Figure S10) confirmed the presence of F, O, P being homogeneously dispersed on the aggregated particles of the cathode and, to a lesser extent C (with atomic% of 17.5%). To sum up, the performance of LFP-Li half cell is characterized by a drop in specific capacity with high C-rates due to the formation of LFP impurity phases, high capacity retention at lower rates, and not grave changes in the LFP morphology upon cycling.

2.3. Graphite-NMC Cell

The cycling behavior of Graphite-NMC cells with and without TFE is shown in Figure S11(a, b) at C/20 and C/10, at room temperature. The voltage window extends from 2.9 to 4.2 V. The cell with the quaternary fluorinated electrolyte reached coulombic efficiencies of ca. 98.9%, same as the standard electrolyte, but unveiled superior discharge capacities, adding ~10 mAh g^{-1} for the investigated C-rates, in line with the results of the pouch cell under the same electrolyte.[17] Such a performance is attributed to the improved i) SEI film resistance and ii) interfacial charge transfer resistance of the cells stemmed from the improved and more accessible ionic associations between Li$^+$ and PF$_6^-$ in the presence of the TFE along with EC and EMC[17] (Table S1), delineated from PEIS.

The Nyquist plots of the Graphite-NMC cells with and without TFE after the initial formation cycle (an example is given in Figure S12a) are presented in Figure S12(b). The ohmic resistance (R_{ohmic}) is the same for both cases reaching 15 ohm (Table S4). The first semicircle witnessed at the high frequencies (70 kHz) represents the solid electrolyte interface (SEI, R_2) and its growth.[17] The second semicircle is wider (and hence more significant) and describes the interfacial and charge transfer processes (R_3). In the presence of TFE, the less broad semicircle denotes a more efficient charge transfer after the formation cycle.[56] The rate capability of the graphite-NMC cell in the presence of the proposed electrolyte is displayed in Figure 3(a). When the current increased from C/20 to 2C, the discharge specific capacity decreased from 150 to 98 mAh g^{-1}. Upon returning to C/5, the capacity retention was ca. 90% after 50 cycles. The values of Figure 3(a) are on par with studies on graphite-NMC cells in the presence of binary carbonate electrolytes and additives (Table S4) and our findings from the Graphite-NMC pouch cells.[17]

Consecutive cycling (Figure 3b, capacity retention at a constant C/5 rate for 100 cycles reaches 83%) leads to an increase of the charge transfer resistance in the bulk electrodes, especially the positive electrode, in the form of a broader second semicircle (Figure 3c), a behavior not uncommon in this battery system.[20] Referring to the PEIS analysis, there is a negligible increase in R_1, suggesting that the SEI layer has not thickened. Hence, cyclable lithium was not heavily consumed in the course of 100 cycles, plausibly because the ternary solvent mixture did not have excess Li, rendering the Li insertion/extraction process more efficient.

FTIR spectroscopy was used in attenuated total reflection (ATR) mode for the characterization of the Celgard separator before and after cycling. The spectra of Figure 3(d) disclose the characteristic peaks of the separator as a quadruple peak at 2951, 2919, 2866, and 2832 Cm^{-1}, single peaks at 1458 and 1379 and 1159 cm^{-1}, and a double peak at 995 and 970 cm^{-1}.[57] When comparing the pristine with the cycled separator (300 h of operation), there were no significant changes in its structure, corroborating its robustness in the presence of the quaternary fluorinated electrolyte on the graphite-NMC cell.

What's more, the distribution of Ni, Co, Mn (in terms of atomic and weight %) was verified by energy-dispersive X-ray spectroscopy (Figure S13). The elemental mapping analysis revealed a somewhat uniform presence of C, O, and F on the cycled NMC surface (Figure S13a). In contrast, for the aged graphite surface (Figure S13b), we witness a separated distribution of C, F, and O elements along with the existence of decomposition products (from the SEM micrograph), similar to one observed in the half-cell study (Figure S2).

The XRD patterns of Figure 4(a, b) compares the state of the pristine and cycled NMC cathode. The absence of the splitting of the (006)/(012) pair of reflections hints at the deterioration of the NMC hexagonal ordering. The I(003)/I(104) peak intensity ratio for the pristine NMC was 1.43 in comparison to 1.81 for the cycled NMC, signifying a change in the bulk structure of the material.[17] Nickel-rich particles are prone to microcracks along grain boundaries that provide gaps for electrolyte
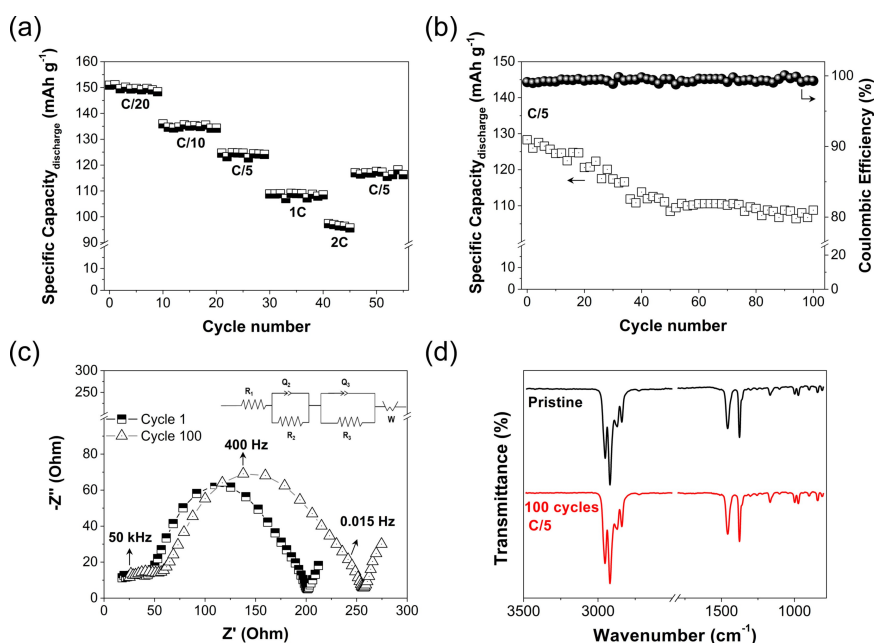
Figure 3. (a) Rate capability and (b) long-term cycling of the Graphite-NMC cell in 0.1 mol L^{-1} LiPF$_6$ in EC/EMC/TFE (3/7/20, wt). The data points in (b) are the average values of three different cells (standard deviation < 8%). (c) Nyquist plots before and after long-term cycling. (d) FTIR spectra of the Celgard separator before and after cycling. Cell operating temperature is 25 °C.
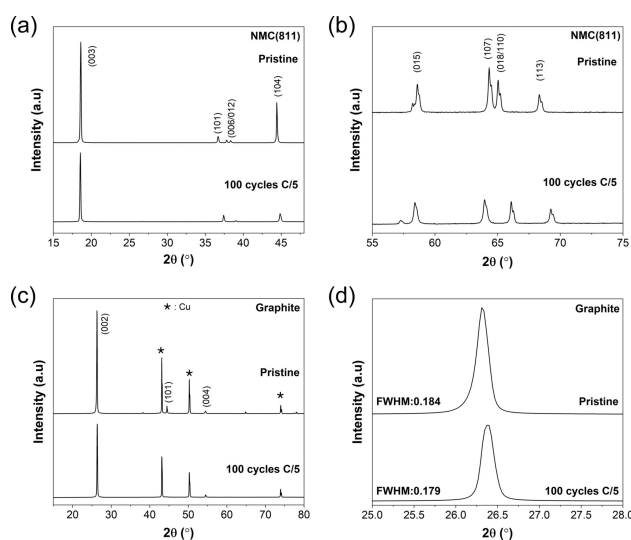

Figure 4. XRD patterns of the (a, b) NMC and (c, d) graphite electrodes before and after cycling (Figure 3b) in a solution containing 0.1 mol L^{-1} LiPF$_6$ in EC/EMC/TFE (3/7/20, wt).

penetration and lead to severe electrolyte oxidation and rock salt formation.[58] Regarding graphite (Figure 4c, d), the XRD patterns show the characteristic (002) sharp diffraction peak, indicative of large crystallite size together with similar peak position and FWHM (i.e., FWHM = 0.184°, for the pristine sample vs. 0.179° for the cycled one). The graphite microcrystalline layer spacing (d002) for the fresh electrode was ca. 0.340 compared to 0.331 of the aged sample.

In summary, on top of the pouch cell architecture, the graphite-NMC coin cells with the nonflammable quaternary fluorinated electrolyte exhibited high coulombic efficiency

(98.9%), good capacity retention (90% at C/5), stability (> 250 cycles at different C-rates), superior performance to the standard electrolyte, and an energy density of 207 Wh kg^{-1} (assuming a nominal voltage of 3.68 V, a total cell weight of 40 mg and a nominal capacity of 2.25 mAh at C/20).

2.4. Graphite-LMO Cell

The electrochemical performance of the graphite-LMO cell was measured within a voltage range of 3.0 to 4.5 V. Initial formation cycles (Figure S14a) were performed with the additional charge (i.e., irreversible capacity) used in the passivation of the active materials (i.e., SEI layer formation together with the extraction/insertion of Li ions).[59] After the formation process, the coulombic efficiency during charge and discharge remains constant, above 98.5%. Figure S14(b) shows the voltage profiles of the graphite-LMO cell at different C-rates, viz., C/20 to 2C. The specific capacity at C/20 reaches 143 mAh g^{-1}, close to the theoretical one of LMO.[20] Upon higher rates (2C), it drops to 82 mAh g^{-1} with the voltage hysteresis in the charge-discharge cycle being almost 1 V (from 55 mV at C/20).

Figure 5(a) presents the cell's differential capacity plots at C/20, unveiling two well-defined anodic and cathodic peaks at 4.02/3.99 V and 3.91/3.82 V vs. Li/Li$^+$. The peaks validate the reversible electrochemical deintercalation/intercalation of Li$^+$ from the tetrahedral sites of LMO taking place in two stages.[60] The first redox pair (3.91/3.82 V) describes the insertion and removal of Li ions from the tetrahedral sites in which Li-Li interactions exist. The second redox pair (4.02/3.99 V) depicts the insertion/removal of Li ions from other tetrahedral sites not
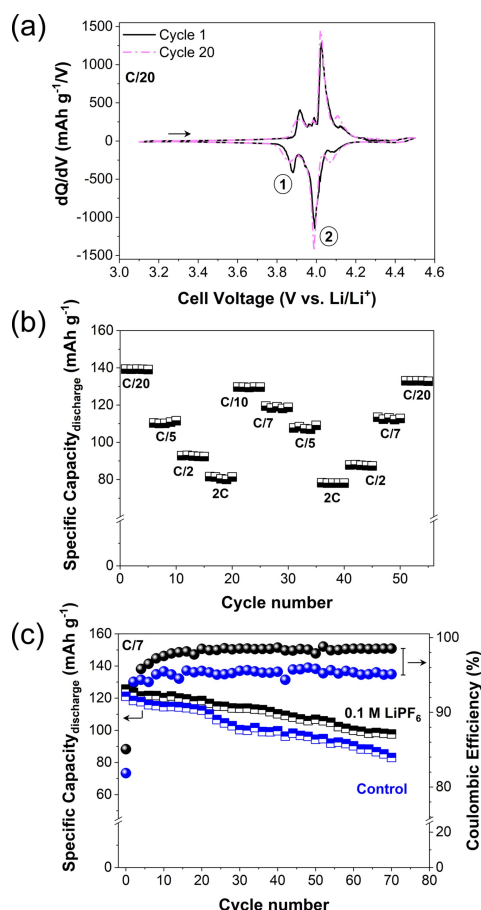
Batteries & Supercaps

Articles
doi.org/10.1002/batt.202100132

Chemistry Europe
European Chemical
Societies Publishing

Figure 5. Electrochemical performance of the Graphite-LMO cell at room temperature in a solution containing 0.1 mol L^{-1} LiPF$_6$ in EC/EMC/TFE (3/7/20, wt). (a) Differential capacity curve, dQ/dV vs. cell voltage at cycle 1 and cycle 20. (b) Rate capability. (c) Specific Capacity and Coulombic efficiency at a C/7 rate. The average values of three different cells are presented here (standard deviation < 8%).

considering the Li-Li interactions.[61] The graphite-LMO cell displayed a stable electrochemical behavior upon repetitive cycling as delineated from the dQ/dV curves of the 1st and 20th cycle.

The rate performance of the Graphite-LMO cell with the formulated electrolyte was investigated at six different rates ranging from C/20 to 2C by cycling it five times at each rate (Figure 5b). The cell achieved average discharge capacities of 139, 128, 121, 110, 90, and 81 mAh g^{-1} at current rates of C/20, C/10, C/7, C/5, C/2, and 2C, respectively. The cell discharge capacity recovered to 132 mAh g^{-1} (94% of its average initial discharge capacity) when the current rate reverted to C/20. Further cycling (Figure S15a, b) demonstrated moderate capacity retention (81% at C/10 and 75% at C/2) after 100 cycles, signifying an enduring spinel LMO crystal structure along with an unaffected Celgard separator (Figure S15c). Figure 5(c) directly compares the performance of the Graphite-LMO cell in the presence of a commercial (i.e., control, 1 mol L^{-1} LiPF$_6$ in EC/EMC, 3/7, v/v) and the quaternary fluorinated electrolyte, validating the latter's superiority both in average coulombic efficiency (98.8% vs. 96%) and capacity retention (77% vs.

70%) for 70 cycles. The coulombic efficiency of the first cycle is higher for the cell containing the quaternary fluorinated electrolyte, viz., 85 to 82%, indicating a more proficient formation cycle (Figure S14a), possibly due to the minimal amount of gas formed as documented in the case of the Graphite-NMC pouch cell.[17] The EDX of the cycled LMO (Figure S16a) points towards a homogeneous and uniform distribution of the C, F, O, and Mn elements. Phosphorus content is feeble, having a normalized atomic percent spectrum of 2.34%. For the anode, the flat surface of graphite (Figure S16b) exhibits irregular polyhedral particles tightly packed with a non-uniform distribution of C, O, and F (i.e., separate regions). Again here, the phosphorus content is low (normalized atomic percent spectrum of 0.56%), yet the presence of bright clusters points to the formation of decomposition products, as previously illustrated in Figure S2.

The XRD patterns of the pristine and cycled LMO cathodes expose sharp peaks, representative of their crystalline and clean nature (Figure 6a, b and Figure S17a–d). The cycled electrodes reveal a slight angle shift and peak broadening, suggesting modest structural changes (i.e., contributions of crystallite size and lattice strain, the latter hinting to material degradation and in turn, reduced capacity retention).[62] The intensity of the (111) peak is the strongest (Figure S17a), corroborated by the I(111)/I(311) ratio of the cycled electrode being 1.5 times higher
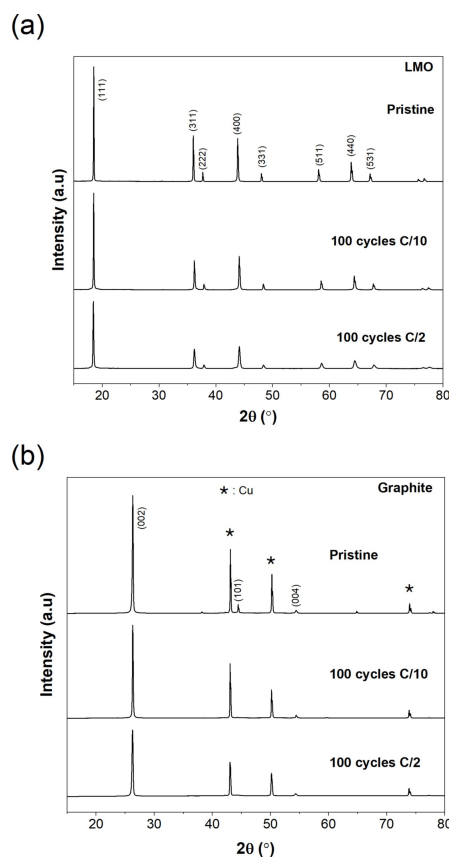

Figure 6. XRD patterns of the (a) LMO and (b) graphite electrodes before and after cycling in a solution containing 0.1 mol L^{-1} LiPF$_6$ in EC/EMC/TFE (3/7/20, wt).

than the pristine (1.81 vs. 1.21), alluding to a preferred orientation along the (111) plane. For the graphite anode, the main (002) peak (i.e., aromatic ring carbon reticulated layers in a three-dimensional arrangement) remained at the same position (26.5°) after cycling, suggesting a constant interlayer spacing of graphite (Figure S17c, d). The pristine graphite shows a higher peak intensity than the cycled electrode (Figure S17c), manifesting its superior crystallinity. The FWHM changed from 0.231° (pristine) to 0.182° (C/2 rate), indicating a deteriorated compact-stacking graphite structure, stemming from graphite volume variation during cycling.[63] The graphite microcrystalline layer spacing (d002) for the pristine electrode was ca. 0.351 compared to 0.328 of the cycled sample.

In short, these results attest to the suitability of the quaternary fluorinated electrolyte for the graphite-LMO cell with good cyclability (200 cycles), high coulombic efficiency (98.8%), modest capacity retention (77%), superior performance to the standard electrolyte and an energy density of 165 Wh kg^{-1} (assuming a nominal voltage of 3.8 V, a total cell weight of 36.5 mg and a nominal capacity of 1.5 mAh at C/20).

2.5. Li Symmetric Cell

Symmetrical Li test cells were further employed to investigate the interfacial characteristics, stability, and rate capability of the formulated electrolyte with Li metal and isolate them from the counter-electrode reactions that would be present in the full cell (i.e., in the absence of oxidative environment). The Li symmetric plot depicts a time versus voltage graph where the overpotential required to remove Li at one electrode and deposit it at the other as a function of time is exposed. Herein, under applied normalized galvanostatic currents of 1.5 and 0.75 mA cm^{-2} with a capacity per unit area of 1 and 0.5 mAh cm^{-2}, respectively (charge-discharge time is one hour), the spatially varying surface kinetics cause a "peaking" shape[64] in the voltage response of Li symmetric cells throughout 600 h, as reflected in Figure 7 and more elaborately in the snapshots of Figure S18.

The voltage peaking behavior, attributed to transition between different kinetic pathways at the electrode/electrolyte
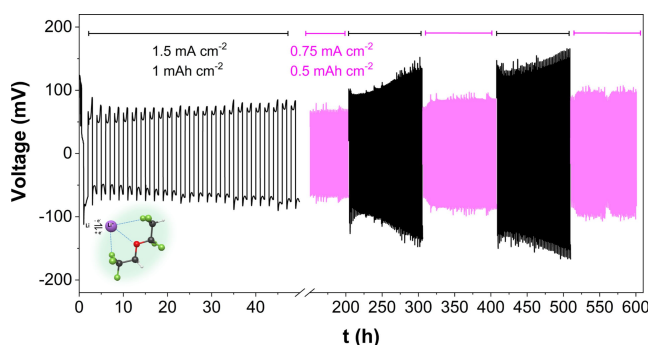

Figure 7. Galvanostatic cycling voltage profile for a Li symmetric coin cell cycled at different current densities in a solution consisting of EC/DMC/TFE and 0.1 mol L^{-1} LiPF$_6$.

interface,[65] is not diminished with an extended cycling period (Figure S18), maintaining its cell capacity. It has been proposed that a change from the "peaking" behavior to an arcing one is associated with a decrease in cell capacity originating from a highly resistive SEI layer.[66,67] Initially, the hysteresis of the Li symmetric cell containing 0.1 mol L^{-1} LiPF$_6$ is less than 200 mV for the current density of 1.5 mA cm^{-2} (Figure S18a–c), followed by a progressive increase to 230 mV (~30 mV) after 250 cycles, yet not approaching failure. As expected, lower current densities lead to a lower hysteresis (i.e., 120 mV for 0.75 mA cm^{-2}, Figure S19d–f).

The increase in total cell polarization with extended cycling can be elucidated by PEIS. Since the reduction potential of the organic-based ternary solvent is below 1 V vs. Li/Li$^+$, when bare Li is exposed to the solution, and a current applied, immediate reactions between Li and electrolyte species are carried out in a time constant of milliseconds or less. SEI effectively prevents further physical contact between Li and the solvent, making Li dynamically stable in certain organic solvents. Yet, the formation of this ionically conductive passivation layer propagates high charge transfer resistance at the SEI-Li interface, portrayed as a large semicircle in Figure S19(a) for the cell containing 0.1 mol L^{-1} LiPF$_6$ and given the symbol R_{ct} (in parallel with a constant phase element, Q_{ct}) on the corresponding EEC (SI, Figure S19b). $R_{solution}$ depicts electrolyte solution, electric contact, and ion conductive resistances. R_{film} corresponds to the surface film resistance (i.e., interfacial resistance of electrolyte/ SEI/Li$^+$ in the high-frequency region).[68,69] The larger diameter of the semicircle connotes higher film resistance of the SEI layer and Li metal.[70] The values derived from the fitting of the equivalent circuit (SI, Table S6) point to a two-fold increase of film and charge transfer resistances upon repetitive cycling, viz. R_{film} and R_{ct} shift from 8.83 and 55.19 ohm to 17.92 and 129.1 ohm, respectively. The electrode surface resistance is far more significant than electrolyte resistance, implying that transport through the SEI is likely to be the prime determinant for the Li overpotential for the stripping/plating rather than the bulk electrolyte conductivity.[71]

Greater LiPF$_6$ concentrations in the Li symmetric cell (e.g., 0.3 M LiPF$_6$, Figure S20a) led to inferior cycling behavior in terms of voltage hysteresis (~600 mV), stability (<100 cycles), and interfacial charge-transfer resistance (Figure S20b, R_{ct} 0.1 M LiPF6 = 55.19 ohm vs. 75.18 and 129 ohm for 0.2 and 0.3 mol L^{-1} LiPF$_6$). R_{ct} is strongly related to the initial state of the Li metal.[65] Since the assembly of the cells is done in a short and parallel timeframe (therefore assuming an identical initial state of the Li metal), the larger LiPF$_6$ quantities boost the oxidation of the Li surface in the early stages of the SEI layer formation and result in a more pronounced passivated film impedance. In addition, Rehnlund et al.[72] calculated that 0.3% of the Li ions in a 1 mol L^{-1} electrolyte are needed to carry a current density of 1 mA cm^{-2}, validating our strategy to use a low concentration. Yet, lowering the Li salt concentration beyond 0.1 mol L^{-1} (e.g., 0.075 mol L^{-1} LiPF$_6$, Figure S20c) gave rise to cell failure, attributed to the low ionic conductivity of the electrolyte (<0.2 mS cm^{-1}) that evoked shorting pathways which in turn add to the formation of dendrites or inactive Li metal.[64] In

Batteries & Supercaps

Articles
doi.org/10.1002/batt.202100132

Chemistry Europe
European Chemical
Societies Publishing

brief, the quaternary fluorinated electrolyte performs in a stable manner for extended periods of cycling ($\sim$600 h) under practical cell operation conditions (i.e., areal current density of 1.5 mA cm^{-2}). Hence, it can be employed in lithium metal batteries.

3. Conclusions

In this study, we validated the performance of LMO, LFP, NMC cathodes, and graphite and Li metal anodes in full and half-cell coin cell configuration in the presence of 0.1 mol L^{-1} LiPF$_6$ dissolved in a nonflammable novel ternary solvent mixture comprising ethylene carbonate (EC), ethyl methyl carbonate (EMC), and 1,1,2,2-tetrafluoroethyl 2,2,2-trifluoroethyl ether (TFE) (3EC/7EMC/20TFE, by weight) (Scheme 1). Taking advantage i) the high TFE polarizability and ii) the excellent coordination of the Li cations with TFE that mitigates the complete dissociation of LiPF$_6$ and solvation of the Li ions by the EC molecule in solution, the cells supported high reversible specific capacities (e.g., LMO$\rightarrow$148 mAh g^{-1}, LFP$\rightarrow$151 mAh g^{-1}), high coulombic efficiencies ($>$98.85%), long calendar life ($>$150 cycles, 80 h), and modest capacity retention (70%–80%). The graphite-NMC and graphite-LMO cells yielded energy densities of 207 and 165 Wh kg^{-1}, respectively, on account of the total cell weight. We noticed the formation of decomposition products with prolonged cycling, especially in the graphite anode and LFP cathode. Still, the distribution of the chemical elements (from EDX) was uniform in most cases. What's more, the quaternary fluorinated electrolyte is compatible with the lithium metal anode as the symmetric cells performed steadily for $\sim$600 h under 1.5 mA cm^{-2} validating the use of the co-solvent electrolyte in LMBs.
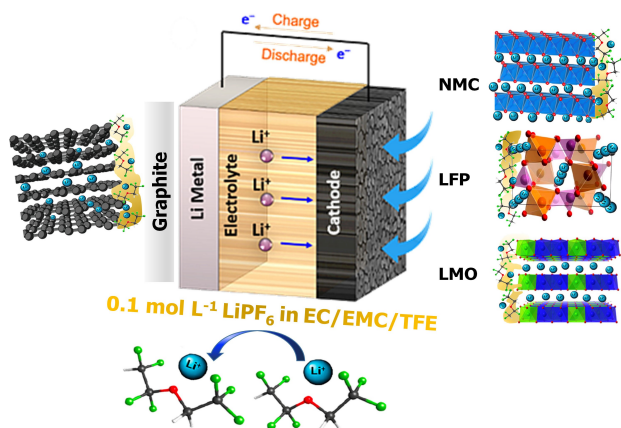
Scheme 1. Quaternary-based fluorinated electrolyte having a record low LiPF$_6$ concentration for LIBs.

Experimental Section

Electrolyte formulation

The electrolyte components in this study were battery-grade ethylene carbonate, EC (Sigma-Aldrich), ethyl methyl carbonate, EMC, and 1,1,2,2-tetrafluoroethyl 2,2,2-trifluoroethyl ether (TFE) (TCI Europe). EC/EMC was formulated at a 3/7 weight ratio. The addition of TFE was based on a 1:2 molar fraction to the EC/EMC binary mixture. The final ternary composition of the electrolyte is (3EC/7EMC/20TFE, wt), abbreviated as (EC/EMC/TFE). A known amount of lithium hexafluorophosphate (LiPF$_6$) salt (Sigma-Aldrich, battery grade) was added to the mixture (Sartorius 1602 MP balance). The electrolyte was formulated in an argon-filled MBraun glovebox at 25°C with a moisture content of $\leq$2 ppm. The water content was measured using an 831 Karl-Fisher Coulometer (Metrohm) and was less than 5 ppm.

Electrolyte characterization

The ionic conductivity (σ) measurements were carried out through a multichannel conductivity meter (Biologic) tailored with a frequency response analyzer (MCS 10, Biologic) and connected to a Peltier-based temperature control unit (10$\rightarrow$80°C, WTSH 10, Biologic). The electrolytes were put into sealed cells with Pt parallel plate electrodes. The viscosity (η) measurements were performed between 10 and 60°C ($\pm$0.02°C) on an Anton Parr rolling-ball viscometer (Lovis 2000 M/ME). The uncertainty of the measurements was ca. 3.5×10^{-5} g cm^{-3} for the density and 2% for the conductivity.

Electrode materials

The NMC (coating weight of 15.7 mg cm^{-2}) and graphite electrodes were supplied by Li-FUN Technology, China. The LMO electrode was supplied from MTI corporation, USA (loading of 10 g cm^{-3}). The LFP electrode was purchased from NEI corporation, USA (loading of 7.3 mg cm^{-2} and press density of 2.0 g cm^{-3}). The graphite electrode was balanced for the N/P ratio between 1.2 and 1.4 for LMO and NMC, respectively. The active surface area, defined as electrode/electrolyte contact area on all electrodes, was 1.77 cm^2. The 15.0 mm discs were cut from the electrode sheets and dried under vacuum at 80°C for 12 h. Then, they were transferred to an Argon-filled glovebox for cell assembly and storage.

Coin cell preparation

The CR2032-type coin cell components were purchased from PI KEM, UK. The cell tests were assembled and sealed (Hohsen Corp. Osaka, Japan) in an Argon-filled glovebox (MBraun, H$_2$O$<$0.1 ppm, O$_2$$<$0.1 ppm). The half-cells tests consisted of LMO, LFP, and NMC as the working electrodes and lithium metal (0.15 g, 200 μm in thickness, Alfa Aesar) as the counter and reference electrode. Two pieces of polypropylene (Celgard 2400, $\phi=25$ μm, porosity$=41$%) were employed as the separator. 150 μL$\pm$10 μL of electrolyte was added dropwise from a micropipette (Mettler-Toledo) between each layer (e.g., 50 μL on the Li metal and 100 μL on the separator). Graphite-NMC and Graphite-LMO cells were assembled in the same manner as the half-cells. For the Li symmetric cells, single pieces of lithium metal foil (0.15 g, 200 μm in thickness, Alfa Aesar, 99% trace metal basis) were used. A WhatmanTM GF/C glass microfiber filter was the separator in this case. Prior to any measurement, the cell remained at open circuit for 12 h at room temperature to form the SEI layer. Then, one formation cycle was implemented at a C/20 charge-discharge rate. To keep the ratio of the electrolyte solution

Batteries & Supercaps

Articles
doi.org/10.1002/batt.202100132

Chemistry Europe
European Chemical
Societies Publishing

to the electrode surface area constant, the same electrolyte volume (viz. 150 μL) was employed for all cells.

Electrochemical investigation

Galvanostatic charge-discharge cycling and cyclic voltammetry were performed using a VMP3 multichannel system (Biologic Science Instrument, France). Triplicate experiments were conducted for all coin cells under galvanostatic charge-discharge with the average value displayed in the Figures 3a, 3b, 5b, 5c below. Potentioelectrochemical impedance spectroscopy (PEIS) for the coin cells was carried out by a VSP-300 Biologic potentiostat (Biologic Science Instrument, France). The AC amplitude was 10 mV, while the frequencies varied between 0.01 Hz and 50 kHz. The nominal values from the electrical equivalent circuit (EEC) are presented in this study. All electrochemical measurements of the coin cells were conducted in a climatic chamber at 25 °C.

Materials characterization

The NMC, LMO, LFP, and graphite electrodes were disassembled in an Argon-filled glovebox (MBraun, $H_2O < 0.1$ ppm, $O_2 < 0.1$ ppm). The samples were washed with EC/EMC solvent and dried accordingly. X-ray diffraction (XRD) patterns were collected from the pristine and used electrodes on a D8 Advance (Bruker) using Ni filtered Cu Kα (1.54 Å, generator: 40 kV, 40 mA) radiation, equipped with a Lynx-eye detector. XRD studies were carried out in a 2θ range from 10° to 90° in continuous mode (step size: ca. 0.02). The morphology of the electrodes before and after cycling was examined at room temperature using a field-emission scanning electron microscope (Zeiss Ultra-55). The distributions of the constituent elements in the composite electrode layers were investigated through an energy-dispersive X-ray (EDX) spectroscopy (X-Max EDS system, Oxford Instruments) with an acceleration voltage of 10 kV. Pristine and cycled Celgard® separators were characterized using Fourier transform infrared spectroscopy (FT-IR, Shimadzu IRAffinity-1S). The FT-IR measurements were performed in air.

Conflict of Interest

The authors declare no conflict of interest.

[1] D. Stampatori, P. P. Raimondi, M. Noussan, *Energies* **2020**, *13*, DOI 10.3390/en13102638.
[2] D. H. Doughty, P. C. Butler, A. A. Akhil, N. H. Clark, J. D. Boyes, *Electrochem. Soc. Interface* **2010**, *19*, 49–53.
[3] Y. Yang, J. Qiu, C. Zhang, J. Zhao, G. Wang, *IEEE Trans. Transp. Electrif.* **2021**, *1*, https://doi.org/10.1109/TTE.2021.3068121.
[4] C. Valant, G. Gaustad, N. Nenadic, *Batteries* **2019**, *5*, 8.
[5] D. Gielen, F. Boshell, D. Saygin, M. D. Bazilian, N. Wagner, R. Gorini, *Energy Strateg. Rev.* **2019**, *24*, 38–50, https://doi.org/10.1016/j.esr.2019.01.006.
[6] A. Phadke, A. Khandekar, D. Wooley, D. Rajagopal, International Energy Analysis Department, Impacts Division, Lawrence Berkeley National Laboratory **2021**, https://eta.lbl.gov/publications/why-regional-long-haul-trucks-are.
[7] D. L. Wood, J. Li, C. Daniel, *J. Power Sources* **2015**, *275*, 234–242.
[8] M. Armand, P. Axmann, D. Bresser, M. Copley, K. Edström, C. Ekberg, D. Guyomard, B. Lestriez, P. Novák, M. Petranikova, W. Porcher, S. Trabesinger, M. Wohlfahrt-Mehrens, H. Zhang, *J. Power Sources* **2020**, *479*, 228708.
[9] J. B. Goodenough, K.-S. Park, *J. Am. Chem. Soc.* **2013**, *135*, 1167–1176.
[10] A. Wang, S. Kadam, H. Li, S. Shi, Y. Qi, *npj Comput. Mater.* **2018**, *4*, 1–26, https://www.nature.com/articles/s41524-018-0064-0.
[11] A. J. Crawford, Q. Huang, M. C. W. Kintner-Meyer, J.-G. Zhang, D. M. Reed, V. L. Sprenkle, V. V. Viswanathan, D. Choi, *J. Power Sources* **2018**, *380*, 185–193.
[12] D. Aurbach, Y. Talyosef, B. Markovsky, E. Markevich, E. Zinigrad, L. Asraf, J. S. Gnanaraj, H.-J. Kim, *Electrochim. Acta* **2004**, *50*, 247–254.
[13] J. Kalhoff, G. G. Eshetu, D. Bresser, S. Passerini, *ChemSusChem* **2015**, *8*, 2154–2175.
[14] V. Aravindan, J. Gnanaraj, S. Madhavi, H. Liu, *Chem. Eur. J.* **2011**, *17*, 14326–14346.
[15] T. R. Jow, K. Xu, O. Borodin, M. Ue, *Electrolytes for Lithium and Lithium-Ion Batteries*, Springer, **2014**.
[16] S. S. Zhang, *J. Power Sources* **2006**, *162*, 1379–1394.
[17] G. Nikiforidis, M. Raghibi, A. Sayegh, M. Anouti, *J. Phys. Chem. Lett.* **2021**, 1911–1917.
[18] X. Fan, L. Chen, O. Borodin, X. Ji, J. Chen, S. Hou, T. Deng, J. Zheng, C. Yang, S.-C. Liou, *Nat. Nanotechnol.* **2018**, *13*, 715–722.
[19] P. Rozier, J. M. Tarascon, *J. Electrochem. Soc.* **2015**, *162*, A2490.
[20] B. Larhrib, G. Nikiforidis, M. Anouti, *Electrochim. Acta* **2021**, *371*, 137841.
[21] G. Zubi, R. Dufo-López, M. Carvalho, G. Pasaoglu, *Renewable Sustainable Energy Rev.* **2018**, *89*, 292–308.
[22] Y. Xie, H.-T. Yu, T.-F. Yi, Y.-R. Zhu, *ACS Appl. Mater. Interfaces* **2014**, *6*, 4033–4042.
[23] J. Asenbauer, T. Eisenmann, M. Kuenzel, A. Kazzazi, Z. Chen, D. Bresser, *Sustain. Energy Fuels* **2020**, *4*, 5387–5416.
[24] B. Liu, J.-G. Zhang, W. Xu, *Joule* **2018**, *2*, 833–845.
[25] G. Nikiforidis, M. C. M. van de Sanden, M. N. Tsampas, *RSC Adv.* **2019**, *9*, 5649–5673.
[26] P. Shi, X. Zhang, X. Shen, R. Zhang, H. Liu, Q. Zhang, *Adv. Mater.* **2020**, *5*, 1900806.
[27] C. L. Berhaut, P. Porion, L. Timperman, G. Schmidt, D. Lemordant, M. Anouti, *Electrochim. Acta* **2015**, *180*, 778–787.
[28] S. Amara, J. Toulc'Hoat, L. Timperman, A. Biller, H. Galiano, C. Marcel, M. Ledigabel, M. Anouti, *ChemPhysChem* **2019**, *20*, 581–594.
[29] M. P. Longinotti, H. R. Corti, *J. Phys. Chem. B* **2009**, *113*, 5500–5507.
[30] C. L. Berhaut, D. Lemordant, P. Porion, L. Timperman, G. Schmidt, M. Anouti, *RSC Adv.* **2019**, *9*, 4599–4608.
[31] A. Byeon, A. M. Glushenkov, B. Anasori, P. Urbankowski, J. Li, B. W. Byles, B. Blake, K. L. Van Aken, S. Kota, E. Pomerantseva, J. W. Lee, Y. Chen, Y. Gogotsi, *J. Power Sources* **2016**, *326*, 686–694.
[32] Z. He, C. Zhang, H. Tang, M. Liu, B. J. Marsden, X. Zhou, *Surf. Interface Anal.* **2021**, *53*, 90–99.
[33] Q. Shi, S. Heng, Q. Qu, T. Gao, W. Liu, L. Hang, H. Zheng, *J. Mater. Chem. A* **2017**, *5*, 10885–10894.
[34] C. Mao, R. E. Ruther, J. Li, Z. Du, I. Belharouak, *Electrochem. Commun.* **2018**, *97*, 37–41.
[35] M. Al-Shroofy, Q. Zhang, J. Xu, T. Chen, A. P. Kaur, Y.-T. Cheng, *J. Power Sources* **2017**, *352*, 187–193.
[36] J. Xu, S.-L. Chou, Q. Gu, H.-K. Liu, S.-X. Dou, *J. Power Sources* **2013**, *225*, 172–178.
[37] Y. Qian, P. Niehoff, M. Börner, M. Grützke, X. Mönnighoff, P. Behrends, S. Nowak, M. Winter, F. M. Schappacher, *J. Power Sources* **2016**, *329*, 31–40.
[38] Y. Wang, J. Roller, R. Maric, *ACS Omega* **2018**, *3*, 3966–3973.
[39] Y. Abe, N. Hori, S. Kumagai, *Energies* **2019**, *12*, DOI 10.3390/en12234507.
[40] A. Aryanfar, D. J. Brooks, A. J. Colussi, M. R. Hoffmann, *Phys. Chem. Chem. Phys.* **2014**, *16*, 24965–24970.
[41] X. Li, J. Liu, M. N. Banis, A. Lushington, R. Li, M. Cai, X. Sun, *Energy Environ. Sci.* **2014**, *7*, 768–778.

[42] L. Liang, X. Sun, C. Wu, L. Hou, J. Sun, X. Zhang, C. Yuan, *ACS Appl. Mater. Interfaces* **2018**, *10*, 5498–5510.

[43] L. Ben, H. Yu, B. Chen, Y. Chen, Y. Gong, X. Yang, L. Gu, X. Huang, *ACS Appl. Mater. Interfaces* **2017**, *9*, 35463–35475.

[44] H. Shin, J. Park, A. M. Sastry, W. Lu, *J. Electrochem. Soc.* **2015**, *162*, A1683–A1692.

[45] D. Tang, Y. Sun, Z. Yang, L. Ben, L. Gu, X. Huang, *Chem. Mater.* **2014**, *26*, 3535–3543.

[46] Y. Xu, G. Chen, E. Fu, M. Zhou, M. Dunwell, L. Fei, S. Deng, P. Andersen, Y. Wang, Q. Jia, H. Luo, *RSC Adv.* **2013**, *3*, 18441–18445.

[47] H. Liu, A. Banerjee, B. Ziv, K. J. Harris, N. P. W. Pieczonka, S. Luski, G. A. Botton, G. R. Goward, D. Aurbach, I. C. Halalay, *ACS Appl. Mater. Interfaces* **2018**, *1*, 1878–1882.

[48] E. Barsoukov, J. R. Macdonald, *Impedance Spectroscopy: Theory, Experiment, and Applications*, John Wiley & Sons, **2018**.

[49] Y. Xiao, X.-D. Zhang, Y.-F. Zhu, P.-F. Wang, Y.-X. Yin, X. Yang, J.-L. Shi, J. Liu, H. Li, X.-D. Guo, B.-H. Zhong, Y.-G. Guo, *Adv. Sci.* **2019**, *6*, 1801908.

[50] H. Zhang, D. Liu, X. Zhang, C. Zhao, Y. Xu, *J. Solid State Electrochem.* **2014**, *18*, 569–575.

[51] A. K. Haridas, C. S. Sharma, N. Y. Hebalkar, T. N. Rao, *Mater. Today* **2017**, *4*, 14–24.

[52] G. Yan, X. Li, Z. Wang, H. Guo, W. Peng, Q. Hu, *J. Solid State Electrochem.* **2016**, *20*, 507–516.

[53] Y. Liu, J. Zhang, Y. Li, Y. Hu, W. Li, M. Zhu, P. Hu, S. Chou, G. Wang, *Nanomaterials* **2017**, *7*, DOI 10.3390/nano7110368.

[54] L. You, J. Tang, Q. Wu, C. Zhang, D. Liu, T. Huang, A. Yu, *RSC Adv.* **2020**, *10*, 37916–37922.

[55] C. Li, Y. Xie, N. Zhang, L. Ai, Y. Liang, K. Tuo, X. Ye, G. Jia, S. Li, *Ionics* **2019**, *25*, 927–937.

[56] I. Landa-Medrano, A. Eguia-Barrio, S. Sananes-Israel, S. Lijó-Pando, I. Boyano, F. Alcaide, I. Urdampilleta, I. de Meatza, *J. Electrochem. Soc.* **2020**, *167*, 90528.

[57] Q. Jiang, Z. Li, S. Wang, H. Zhang, *RSC Adv.* **2015**, *5*, 92995–93001.

[58] S. Ge, Y. Leng, T. Liu, R. S. Longchamps, X.-G. Yang, Y. Gao, D. Wang, D. Wang, C.-Y. Wang, *Sci. Adv.* **2020**, *6*, eaay7633.

[59] M. Bakierska, M. Świętosławski, R. Dziembaj, M. Molenda, *Mater. (Basel, Switzerland)* **2016**, *9*, DOI 10.3390/ma9080696.

[60] M. M. Thackeray, *Prog. Solid State Chem.* **1997**, *25*, 1–71.

[61] J.-Y. Luo, X.-L. Li, Y.-Y. Xia, *Electrochim. Acta* **2007**, *52*, 4525–4531.

[62] A. A. Al-Tabbakh, N. Karatepe, A. B. Al-Zubaidi, A. Benchaabane, N. B. Mahmood, *Int. J. Energy Res.* **2019**, *43*, 1903–1911.

[63] G. Wang, F. Wang, P. Zhang, J. Zhang, T. Zhang, K. Müllen, X. Feng, *Adv. Mater.* **2018**, *30*, 1802949.

[64] K.-H. Chen, K. N. Wood, E. Kazyak, W. S. LePage, A. L. Davis, A. J. Sanchez, N. P. Dasgupta, *J. Mater. Chem. A* **2017**, *5*, 11671–11681.

[65] K. N. Wood, E. Kazyak, A. F. Chadwick, K.-H. Chen, J.-G. Zhang, K. Thornton, N. P. Dasgupta, *ACS Cent. Sci.* **2016**, *2*, 790–801.

[66] E. Kazyak, K. N. Wood, N. P. Dasgupta, *Chem. Mater.* **2015**, *27*, 6457–6462.

[67] D. Lu, Y. Shao, T. Lozano, W. D. Bennett, G. L. Graff, B. Polzin, J. Zhang, M. H. Engelhard, N. T. Saenz, W. A. Henderson, *Adv. Energy Mater.* **2015**, *5*, 1400993.

[68] A. Zaban, E. Zinigrad, D. Aurbach, *J. Phys. Chem.* **1996**, *100*, 3089–3101.

[69] H. Lee, H. Song, Y.-J. Kim, J.-K. Park, H.-T. Kim, *Sci. Rep.* **2016**, *6*, 1–10.

[70] G. Bieker, M. Winter, P. Bieker, *Phys. Chem. Chem. Phys.* **2015**, *17*, 8670–8679.

[71] X. Cheng, R. Zhang, C. Zhao, F. Wei, J. Zhang, Q. Zhang, *Adv. Sci.* **2016**, *3*, 1500213.

[72] D. Rehnlund, C. Ihrfors, J. Maibach, L. Nyholm, *Mater. Today* **2018**, *21*, 1010–1018.